# Comparison among translational temperatures of $\mathrm{He}(^1P^{\mathrm{o}}_1)$, $\mathrm{He}(^3S_1)$, and $\mathrm{Ar}(4s[3/2]^{\mathrm{o}}_2)$ in inductively coupled plasmas

Kosuke Takada[1], Shusuke Nishiyama[2], and Koichi Sasaki[1]*

[1] *Division of Applied Quantum Science and Engineering, Hokkaido University, Kita 13, Nishi 8, Kita-ku, Sapporo 060-8628, Japan*

[2] *Faculty of Health Science, Japan Healthcare University, 1-50, 11-choume, Tsukisamu-Higashi 3-jo, Toyohira-ku, Sapporo, 062-0053, Japan*

We compared the translational temperatures of $\mathrm{He}(^1P^{\mathrm{o}}_1)$, $\mathrm{He}(^3S_1)$, and $\mathrm{Ar}(4s[3/2]^{\mathrm{o}}_2)$ in low-pressure inductively coupled plasmas. We employed laser absorption spectroscopy for measuring the Doppler broadening widths of the transition lines, and they told us the translational temperatures of the three electronic excited states. From the comparison between the temperatures of $\mathrm{He}(^1P^{\mathrm{o}}_1)$ and $\mathrm{He}(^3S_1)$, we confirmed that the metastable $^3S_1$ state can work as the probe for the temperature measurement of the ground-state helium atoms. We observed higher temperatures for $\mathrm{Ar}(4s[3/2]^{\mathrm{o}}_2)$ than $\mathrm{He}(^3S_1)$ in helium-argon mixture plasmas with total pressures less than 80 mTorr. The higher $\mathrm{Ar}(4s[3/2]^{\mathrm{o}}_2)$ temperature is considered to be due to the selective heating of argon by the charge exchange collision with $Ar^+$.

## 1. Introduction

The gas temperature is an important parameter in low-temperature plasmas. It directly affects the density of neutral species if the gas pressure is controlled at a constant value. The density of neutral species affects the electron temperature and the electron density in the plasma.[1)] Accordingly, the gas temperature links with the basic plasma parameters in low-temperature plasmas. When the plasma is produced using molecular gas, the densities of reactive radicals are affected by the gas temperature, since the production process of reactive radicals is governed by electron impact dissociation of neutral species in low-temperature plasmas. In addition, the rate coefficients of chemical reactions between neutral species are sensitive to the gas temperature. Since the transport of neutral species works as a major thermal flux to the material surface, the gas temperature also influences the rates of surface reaction processes. Hence, the gas temperature is especially important when a low-temperature reactive plasma is utilized for material processing.

*Corresponding author, E-mail: sasaki@qe.eng.hokudai.ac.jp

Various methods are used for measuring gas temperatures in low-temperature plasmas. A widely used method is based on the assumption that the translational temperature of a molecular species is equal to its rotational temperature.[2–7] Thanks to spectral simulation software such as Specair and Lifbase, in the case of diatomic molecules, it is quite easy for researchers, who do not have deep knowledge of molecular spectroscopy, to estimate the rotational temperature by observing the optical emission spectrum. However, the optical emission spectrum of an diatomic molecule tells us the rotational temperature of an electronic excited state. If we use broadband absorption spectroscopy,[8–10] laser absorption spectroscopy,[11,12] laser-induced fluorescence,[13–17] and laser Raman scattering,[18–20] it is possible to measure the rotational population distribution of the electronic ground state, and in this case we can estimate its rotational temperature. However, we still need the assumption that the rotational temperature of the electronic ground state is equal to the translational temperature of the molecule.

The measurement of the translational temperature is possible by measuring the Doppler broadening width of the transition line. We can measure the spectral profile of an optical emission line using a Fabry-Perot interferometer with a fine spectral resolution.[21,22] However, the Doppler broadening width of the spectral profile represents the translational temperature of an electronic excited state. Laser absorption spectroscopy is the method with the finest spectral resolution for measuring the spectral line profile. The spectral line profile of a vibrational-rotational transition, which is detected using a mid-infrared diode laser, can be used for measuring the translational temperature of a molecular species at the electronic ground state.[23] The measurement of the spectral line profile of the resonance line of an atomic species is possible only for metal atoms[24–26] and silicon,[27] since commercially available tunable laser sources are limited in infrared, visible, and ultraviolet wavelength ranges. In the case of light elements and rare gases, the lower energy state of the transition line in laser absorption spectroscopy is usually a metastable state,[28–31] and we need to check the coincidence between the temperatures of the metastable and ground states. In addition, in the case of a plasma with multiple neutral species, it is doubtful whether the temperature of an atom or a molecule is the representative gas temperature or not, and we need to check the coincidence among the translational temperatures of multiple species.

In this work, we adopted laser absorption spectroscopy for the measurement of the gas temperature in an inductively coupled plasma source. We measured the translational temperatures of He($^1P_1^o$), He($^3S_1$), and Ar($4s[3/2]_2^o$). The $^1P_1^o$ state of helium is a radiative state, whereas the $^3S_1$ and $4s[3/2]_2^o$ are metastable states of helium and argon, respectively. Since the temperature of the He($^1P_1^o$) state is considered to be equal to the temperature of the ground

state because of the radiation trapping process, we examined the validity of the metastable $^3S$ state as the probe for the gas temperature measurement by comparing the temperatures of He($^1P_1^o$) and He($^3S_1$). In addition, after checking the validity of He($^3S_1$) for the measurement of the helium temperature, we compared the temperatures of the metastable states of helium ($^3S_1$) and argon ($4s[3/2]_2^o$) in helium-argon mixture plasmas. We compared the temporal variations of the translational temperatures, and we discussed the heating kinetics in the mixture plasma.

## 2. Experiment

The experimental apparatus is shown in Fig. 1. Helium or helium-argon mixture plasma was produced in a cylindrical vacuum chamber with a diameter and a height of 26 cm. A one-turn rf antenna was inserted into the vacuum chamber, and it was connected to an rf power supply at 13.56 MHz via a matching circuit. The rf antenna was electrically insulated from the plasma by covering its surface with glass fibers. The vacuum chamber was evacuated using a turbo molecular pump below $4 \times 10^{-6}$ Torr. After the evacuation, pure helium or the mixture of helium and argon was introduced into the vacuum chamber via mass flow controllers. The flow rate of helium was 73 sccm in the pure helium discharge. The flow rate of helium was kept at the same value in the helium-argon mixture plasma, and we added argon with a smaller flow rate to realize the partial pressure ratio of $P_{\mathrm{He}} : P_{\mathrm{Ar}} = 20 : 1$. This partial pressure ratio was chosen to realize similar absorption strengths at the $^3S_1 - ^3P_0^o$ transition of helium and the $4s[3/2]_2^o - 4p[3/2]_2$ transition of argon. The gas pressure was measured using a capacitance manometer, and it was controlled by controlling the pumping speed using a gate valve.

We used three tunable diode lasers in this experiment. The wavelengths of the diode lasers were 667.82 nm (for the absorption from the $^1P_1^o$ to $^1D_2$ states of helium), 1082.91 nm (for the absorption from the $^3S_1$ to $^3P_0^o$ states of helium), and 763.51 nm (for the absorption from the $4s[3/2]_2^o$ to $4p[3/2]_2$ states of argon). Two of the three diode lasers were installed in the system shown in Fig. 1. The two diode laser beams were superposed on the same optical axis using a beam splitter. The superposed laser beams were introduced into an optical fiber, and it guided the laser beams to the vacuum chamber. The laser beams yielded from the optical fiber were collimated, and they were injected into the plasma. The laser beams transmitted through the plasma were separated into two optical passes using another beam splitter, and they were detected using photodiodes. Interference filters which had the transmissions at the laser wavelengths were placed in front of the photodiodes. In this way, we measured the optical absorption at the two transition lines at the same position in the plasma. In the

measurement in the steady-state plasma, we observed the optical absorption spectra of the two transition lines simultaneously. The wavelengths of the two diode lasers were scanned slowly with time, and the variations of the transmitted laser intensities were recorded using an oscilloscope. The variations of the laser wavelengths were measured using Fabry-Perot spectrum analyzers. For measuring the temporal variations of the absorption spectra in the pulsed plasma, which had a duration of 100 ms and a repetition frequency of 5 Hz, we measured the temporal variation of absorption at a fixed laser wavelength in a transition line. The measurement of the temporal variation of absorption was repeated at various wavelengths, so that we obtained the temporal variation of the absorption spectrum. The measurements of the absorption spectra in the afterglow were possible for metastable He($^3S_1$) and Ar($4s[3/2]^o_2$), whereas it was impossible for radiative He($^1P^o_1$) because of the low density. A longer time was necessary to complete this complicated measurement, and the measurements at the two transition lines were not simultaneous. The powers of the diode laser beams were lower than 50 $\mu$W, which was weak enough to avoid the saturation of absorption.

## 3. Spectral analysis

The absorption spectrum thus obtained was fitted with theoretical spectrum to deduce the translational temperature. We employed a Voigt profile for the theoretical spectrum in the spectral fitting of the $^1P^o_1$–$^1D_2$ transition line of helium. This is because the natural broadening width of this transition is approximately 0.3 GHz, which is not negligible in comparison with the Doppler broadening width ($\sim$ 3 GHz). The difference between the gas temperatures deduced by assuming the Voigt and Gaussian profiles was approximately 10% in the $^1P^o_1 - ^1D_2$ transition line. The natural broadening widths of the $^3S_1 - ^3P^o_0$ transition of helium and the $4s[3/2]^o_2 - 4p[3/2]_2$ transition of argon are 0.015 and 0.017 GHz, respectively. Since these natural broadening widths are much narrower than the Doppler broadening widths, we employed the Gaussian profiles for the analyses of the absorption spectra of these transition lines. We confirmed that the same translational temperatures were obtained by assuming the Voigt and Gaussian profiles for the $^3S_1 - ^3P^o_0$ transition of helium.

## 4. Results

### 4.1 Comparison between translational temperatures of He($^1P^o_1$) and He($^3S_1$)

Figures 2(a) and 2(b) show the absorption spectra of the $^1P^o_1 - ^1D_2$ and $^3S_1 - ^3P^o_0$ transition lines of helium, respectively. The measurements were carried out in a steady-state plasma produced at an rf power of 700 W and a helium pressure of 50 mTorr. The origins of the

horizontal axes correspond to the line centers of the transition lines. The vertical axes are given by $-\ln(I_t/I_0)$, where $I_0$ and $I_t$ are the intensities of incident and transmitted laser beams, respectively. The plots show the experimental results and the solid curves are the fittings using the Voigt (Fig. 2(a)) and Gaussian (Fig. 2(b)) profiles. The precise fittings were obtained as shown in Fig. 2. The translational temperatures of 410 and 400 K were deduced for He($^1P_1^o$) and He($^3S_1$), respectively, by the spectral fittings.

Figure 3 shows the comparison between the translational temperatures of He($^1P_1^o$) and He($^3S_1$). The experimental data were obtained at rf powers between 300 and 700 W and helium pressures between 20 and 150 mTorr. We observed the increase in the He($^1P_1^o$) and He($^3S_1$) temperatures with both the rf power and the helium pressure. As shown in the figure, almost the same translational temperatures were observed for He($^1P_1^o$) and He($^3S_1$) at various discharge conditions of the steady-state helium plasmas.

The evolutions of the translational temperatures of He($^1P_1^o$) and He($^3S_1$) in a pulsed plasma are shown in Figs. 4(a) and 4(b), respectively. The rf power and the helium pressure were 500 W and 80 mTorr, respectively. The rf power was switched on at the origins of the horizontal axes, and we observed the temporal variations of the translational temperatures after the initiation of the discharge. The plots are the experimental results, and the solid curves represent the fittings using

$$T(t) = T_0 + \Delta T \left\{1 - \exp\left(\frac{t}{\tau}\right)\right\}, \tag{1}$$

where $T_0$ is the temperature before the initiation of the discharge, $\Delta T$ is the magnitude of the temperature increase, and $\tau$ is the time constant in the temperature evolution. $T_0 = 300$ K is assumed in Fig. 4. The experimental results were fitted well by the exponential functions, as shown in the figure. The time constants $\tau$ were almost the same, and were 1.04 and 1.09 ms for He($^1P_1^o$) and He($^3S_1$), respectively. The magnitude of the temperature increase $\Delta T$ were 150 and 130 K for He($^1P_1^o$) and He($^3S_1$), respectively.

### 4.2 Comparison between translational temperatures of He($^3S_1$) and Ar($4s[3/2]_2^o$)

The absorption spectra of the $4s[3/2]_2^o - 4p[3/2]_2$ transition line of argon were fitted well by Gaussian functions. We deduced the translational temperatures of He($^3S_1$) and Ar($4s[3/2]_2^o$) in the helium-argon mixture plasmas from the Doppler broadening widths. Figure 5 shows the translational temperatures of He($^3S_1$) and Ar($4s[3/2]_2^o$) as a function of the total pressure. The rf power was fixed at 500 W. As shown in the figure, we observed the same translational temperatures at pressures higher than 80 mTorr. On the other hand, when the pressure was lower than 80 mTorr, the translational temperature of Ar($4s[3/2]_2^o$) was higher than that of He($^3S_1$).

The difference between the temperatures was larger at a lower pressure. Figure 6 shows the comparison between the translational temperatures of He($^3S_1$) and Ar($4s[3/2]^o_2$) observed at various rf powers and three pressures of 10, 50, and 100 mTorr. We observed the increases in the translational temperatures with the rf power for both He($^3S_1$) and Ar($4s[3/2]^o_2$). As shown in the figure, the same temperatures were observed at various rf powers when the pressure was 100 mTorr. On the other hand, when the pressures were 10 and 50 mTorr, the translational temperature of Ar($4s[3/2]^o_2$) was higher than that of He($^3S_1$) at all the rf powers.

Figure 7 shows the temporal variations of the translational temperature and the density of He($^3S_1$) in the afterglow of a pulsed discharge. The rf power in the discharge phase was 200 W and the total pressure was 50 mTorr. The horizontal axes show the delay time after the termination of the rf power. The decrease in the density of He($^3S_1$) shown in Fig. 7(b) was approximated roughly by an exponential function, and the lifetime of He($^3S_1$) was evaluated to be 0.32 ms. Figure 8 shows the temporal variations of the translational temperature and the density of Ar($4s[3/2]^o_2$) in the afterglow of the pulsed discharge produced at the same discharge conditions. The temporal variation of the temperature of Ar($4s[3/2]^o_2$) was more complicated than that of He($^3S_1$), as shown in Fig. 8(a). A steep decrease in the temperature was observed in the initial afterglow, and after that we observed roughly constant temperature until 1.5 ms after the termination of the rf power. The decay of the Ar($4s[3/2]^o_2$) density was not approximated by a single exponential function. We observed a higher Ar($4s[3/2]^o_2$) density than that expected by an exponential decrease in the late afterglow. The difference between the temperatures of He($^3S_1$) (Fig. 7(a)) and Ar($4s[3/2]^o_2$) (Fig. 8(a)) in the discharge phase was greater than those expected from Figs. 5 and 6, which may be due to the fact that the two measurements were not simultaneous. The measurement of the Ar($4s[3/2]^o_2$) temperature was carried out after finishing the measurement of the He($^3S_1$) temperature. The temperature of the vacuum chamber was higher when we measured the Ar($4s[3/2]^o_2$) temperature, and the Ar($4s[3/2]^o_2$) temperature may be affected by the temperature of the vacuum chamber.

## 5. Discussion

### 5.1 Validity of translational temperature of metastable state for gas temperature measurement

The $^3S_1$ state of helium is a metastable state. On the other hand, the $^1P^o_1$ state of helium is a radiative state which decays into the $^1S$ state (the ground state) by emitting photons at a wavelength of 58.43 nm. Since the transition probability of this transition line is $1.8 \times 10^9$ $s^{-1}$,[32] the ground-state helium atoms absorb the photons and go back to the $^1P^o_1$ state with

a high probability. Because of the high exchange rate between the $^1P_1^o$ and $^1S$ states due to the radiation trapping, we can expect the same translational temperatures for these states. On the basis of the coincidence between the translational temperatures of He($^1P_1^o$) and He($^3S_1$) (Fig. 3), we can say that the translational temperature of the metastable $^3S_1$ state represents the translational temperature of the ground state.

The coincidence between the translational temperatures of He($^1P_1^o$) and He($^3S_1$) is reasonable considering the mean free path of helium atoms. Since the transition probability of the forbidden $^1S_0 - ^3S_1$ transition is $1.3 \times 10^{-4}$ s$^{-1}$,[32] He($^3S_1$) can collide with helium during the transport to the chamber wall. The cross section for the collision is estimated to be $2.5 \times 10^{-19}$ m$^2$ on the basis of the van der Waals radius.[33,34] This cross section results in a mean free path of 8 mm at a helium atom density corresponding to a pressure of 20 mTorr (the lowest pressure in the experiment using pure helium). Since the mean free path is more than one-order of magnitude shorter than the radius of the vacuum chamber (13 cm), it is reasonable to observe the same translational temperatures for the metastable and ground states. The coincidence between the temperatures of the metastable and ground states should be examined in a future work at discharge conditions where the mean free path is comparable to the radius of the vacuum chamber.

### 5.2 Mechanism for different translational temperatures of helium and argon

The $4s[3/2]_2^o$ state of argon is a metastable state. However, "the metastability" of Ar($4s[3/2]_2^o$) is low in plasmas due to the following reason. The $4s[3/2]_2^o$ state is exchanged with $4s[3/2]_1^o$ by electron impact (Ar($4s[3/2]_2^o$) + e $\rightarrow$ Ar($4s[3/2]_1^o$) + e). The rate coefficient for this reaction is $2 \times 10^{-7}$ cm$^3$/s.[35] Hence, in a plasma with an electron density of $1 \times 10^{11}$ cm$^{-3}$, which is the value measured using a Langmuir probe, the frequency of the exchange between the $4s[3/2]_2^o$ and $4s[3/2]_1^o$ states amounts to $2 \times 10^4$ s$^{-1}$. The $4s[3/2]_1^o$ state decays into the $^1S$ state (the ground state) by emitting photons at a wavelength of 106.67 nm. Since the transition probability of this transition line is $1.3 \times 10^8$ s$^{-1}$,[32] the ground-state argon atoms absorb the photons and go back to the $4s[3/2]_1^o$ state. Accordingly, the $4s[3/2]_2^o$ state is exchanged with the ground state, and the exchange frequency is higher than the reciprocal of the radiative lifetime of Ar($4s[3/2]_2^o$).[32] Therefore, it is reasonable to consider that the translational temperature of Ar($4s[3/2]_2^o$) represents the temperature of ground-state argon atoms.

As shown in Figs. 6 and 7, we observed higher temperatures for argon than helium when the total pressure was lower than 80 mTorr. The most fundamental heating process for ground-state helium and argon is elastic collision with electron, and the energy transfer from electron

is more efficient for helium than argon because of the smaller mass. In addition, the cross section for collision between helium and argon is estimated to be $3.4 \times 10^{-19}$ m$^2$ on the basis of the van der Waals radii,[33,34] corresponding to a mean free path of 2.4 mm at a pressure of 50 mTorr. Since the mean free path is much shorter than the radius of the vacuum chamber, it is natural to expect the same temperatures for helium and argon. However, the experimental result contradicts this expectation.

A hint to understand the mechanism for the different translational temperatures between helium and argon is seen in Fig. 8(a). The time constant for the decrease in the Ar($4s[3/2]^o_2$) temperature in the initial afterglow is approximately 40 $\mu$s, which is much shorter than the decay time constant of the He($^3S_1$) temperature. The rapid decay of the Ar($4s[3/2]^o_2$) temperature in the initial afterglow suggests the disappearance of a selective heating mechanism for argon by the termination of the rf power. We speculate that the charge exchange collision between argon and $Ar^+$ is the selective heating mechanism. As shown in Figs. 7(b) and 8(b), the density of He($^3S_1$) was approximately five times higher than that of Ar($4s[3/2]^o_2$) in the discharge phase. Considering the pressure ratio of $P_{He} : P_{Ar} = 20 : 1$, the density ratio of the metastable to ground states is higher in argon than helium, which may be due to the lower excitation energy of Ar($4s[3/2]^o_2$) than He($^3S_1$). By referring to this experimental result and considering the fact that the ionization potential of argon is also lower than that of helium, we can expect that the degree of ionization is higher for argon than helium. If the $Ar^+$ temperature is higher than the argon temperature, the charge exchange collision can be a selective heating mechanism for argon. The cross section for charge exchange collision is $6.1 \times 10^{-19}$ m$^2$,[36] corresponding to a mean free path of 2.8 cm at a total pressure of 50 mTorr (the partial pressure of argon is 2.4 mTorr). This mean free path is one-fifth of the radius of the vacuum chamber, but it is longer than the mean free path for the collision between helium and argon. If we assume 0.1 eV for the $Ar^+$ temperature for example, the frequency of the charge exchange collision amounts to $2.8 \times 10^4$ s$^{-1}$. This collision frequency is consistent with the time constant (40 $\mu$s) for the decrease in the Ar($4s[3/2]^o_2$) temperature in the initial afterglow. The total pressure higher than 80 mTorr probably results in similar temperatures of argon and $Ar^+$ since the mean free path of the charge exchange collision is much shorter than the radius of the vacuum chamber. In addition, the relaxation of the Ar($4s[3/2]^o_2$) temperature by the collision with helium becomes important at pressures higher than 80 mTorr, and in this case we observe the same temperatures for helium and argon.

The assumption of the higher ionization degree for argon is consistent with the temporal variations of the density and the temperature of Ar($4s[3/2]^o_2$) in the late afterglow (Fig. 8).

We can suppose two mechanisms for the higher Ar($4s[3/2]^o_2$) density than that expected by an exponential function in the late afterglow: the decrease in the electron impact quenching rate due to the decrease in the electron density and the production of argon via three-body recombination between $Ar^+$ and low-energy electron ($Ar^+ + e + e \rightarrow Ar + e$). We cannot judge which process is more important for the higher Ar($4s[3/2]^o_2$) density in the late afterglow on the basis of Fig. 8(b). On the other hand, the roughly constant temperature of Ar($4s[3/2]^o_2$) shown in Fig. 8(a) suggests the existence of a heating mechanism in the late afterglow. The heating in the late afterglow is consistent with the production of argon by three-body recombination since it links the argon temperatures to the temperature of $Ar^+$. In contrast to Ar($4s[3/2]^o_2$), as shown in Fig. 7, we detect no signs of the production of helium by three-body recombination between $He^+$ and electron, suggesting a lower ionization degree for helium than argon.

## 6. Conclusions

In this work, we compared the translational temperatures of He($^1P^o_1$), He($^3S_1$), and Ar($4s[3/2]^o_2$) in low-pressure (10-150 mTorr) inductively coupled plasmas. From the comparison between the temperatures of He($^1P^o_1$) and He($^3S_1$), we confirmed that the temperature of the metastable $^3S_1$ state represents the temperature of helium at the ground state. We observed higher temperatures for Ar($4s[3/2]^o_2$) than He($^3S_1$) in helium-argon mixture plasmas with total pressures less than 80 mTorr. The higher Ar($4s[3/2]^o_2$) temperature is considered to be due to the selective heating of argon by the charge exchange collision. Similar selective heating mechanisms may be available in other plasmas, if the plasmas are composed of atomic and/or molecular species with remarkably different ionization potentials. The present experimental result could be a remarkable attention to the general assumption that the temperatures of all neutral species are the same in low-temperature, low-pressure plasmas.

## References


1) M. A. Lieberman and A. J. Lichtenberg, *Principles of Plasma Discharges and Materials Processing, 2nd ed.* (Wiley-Interscience, 2005).
2) P. J. Bruggeman, N. Sadeghi, D. C. Schram, and V. Linss, Plasma Sources Sci. Technol. **23**, 023001 (2014).
3) V. M. Donnelly and M. V. Malyshev, Appl. Phys. Lett. **77**, 2467 (2000).
4) T. Sakamoto, H. Matsuura, and H. Akatsuka, J. Appl. Phys. **101**, 023307 (2007).
5) P. Bruggeman, F. Iza, P. Guns, D. Lauwers, M. G. Kong, Y. A. Gonzalvo, C. Leys, and D. C. Schram, Plasma Sources Sci. Technol. **19**, 015016 (2009).
6) T. Silva, N. Britun, T. Godfroid, and R. Snyders, Plasma Sources Sci. Technol. **23**, 025009 (2014).
7) A. Lo, A. Cessou, P. Boubert, and P. Vervisch, J. Phys. D: Appl. Phys. **47** 115201 (2014).
8) J. P. Booth, G. Cunge, F. Neuilly, and N. Sadeghi, Plasma Sources Sci. Technol. **7**, 423 (1998).
9) N. Bulcourt, J. P. Booth, E. A. Hudson, J. Luque, D. K. W. Mok, E. P. Lee, F.-T. Chau, and John M. Dyke, J. Chem. Phys. **120**, 9499 (2004).
10) Y. Du, G. Nayak, G. Oinuma, Y. Ding, Z. Peng, and P. J. Bruggeman, Plasma Sources Sci. Technol. **26**, 095007 (2017).
11) W. M. M. Kessels, J. P. M. Hoefnagels, M. G. H. Boogaarts, D. C. Schram, and M. C. M. van de Sanden, J. Appl. Phys. **89**, 2065 (2001).
12) P. Macko, G. Cunge, and N. Sadeghi, J. Phys. D: Appl. Phys. **34**, 1807 (2001).
13) G. A. Hebner, J. Appl. Phys. **89**, 900 (2001).
14) K. L. Steffens and M. A. Sobolewski, J. Appl. Phys. **96**, 71 (2004).
15) Y. Nakagawa, R. Ono, and T. Oda, J. Appl. Phys. **110**, 073304 (2011).
16) A. F. H. van Gessel, B. Hrycak, M. Jasiński, J Mizeraczyk, J. J. A. M. van der Mullen, and P. J. Bruggeman, J. Phys. D: Appl. Phys. **46**, 095201 (2013).
17) H. Ishigame, S. Nishiyama, and K. Sasaki, Jpn. J. Appl. Phys. **54**, 01AF02 (2015).
18) A. F. H. van Gessel, E. A. D. Carbone, P. J. Bruggeman, and J. J. A. M. van der Mullen, Plasma Sources Sci. Technol. **21**, 015003 (2012).
19) F. Brehmer, S. Welzel, B. L. M. Klarenaar, H. J. van der Meiden, M. C. M. van de Sanden, and R. Engeln, J. Phys. D: Appl. Phys. **48** 155201 (2015).
20) B. L. M. Klarenaar, M. Grofulović, A. S. Morillo-Candas, D. C. M. van den Bekerom,

M. A. Damen, M. C. M. van de Sanden, O. Guaitella, and R, Engeln, Plasma Sources Sci. Technol. **27**, 045009 (2018).

21) N. Britun, M. Gaillard, S.-G. Oh, and J. G. Han, J. Phys. D: Appl. Phys. **40**, 5098 (2007).
22) S. Löhle and S. Lein, Rev. Sci. Instrum. **83**, 053111 (2012).
23) J. Röpcke, G. Lombardi, A. Rousseau, and P. B. Davies, Plasma Sources Sci. Technol. **15**, S148 (2006).
24) H. Scheibner, St. Franke, S. Solyman, J. F. Behnke, C. Wilke, and A. Dinklage, Rev. Sci. Instrum. **73**, 378 (2002).
25) C. Vitelaru, L. de Poucques, T. M. Minea, and G. Popa, J. Appl. Phys. **109**, 053307 (2011).
26) M. Inoue, T. Ohta, N. Takota, S. Tsuchitani, M. Ito, S. Takashima, H. Kano, K. Yamakawa, K. Takeda, and M. Hori, Jpn. J. Appl. Phys. **51**, 086301 (2012).
27) M. Hiramatsu, M. Sakakibara, M. Mushiga, and T. Goto, Meas. Sci. Technol. **2**, 1017 (1991).
28) J. M. Williamson, P. Bletzinger, and B. N. Ganguly, J. Phys. D: Appl. Phys. **37**, 1658 (2004).
29) S. G. Belostotskiy, V. M. Donnelly, D. J. Economou, and N. Sadeghi, IEEE Trans. Plasma Sci. **37**, 852 (2009).
30) C. Vitelaru, D. Lundin, G. D. Stancu, N. Brenning, J. Bretagne, and T. Minea, Plasma Sources Sci. Technol. **21**, 025010 (2012).
31) V. Sushkov, H. T. Do, M. Cada, Z. Hubicka, and R. Hippler, Plasma Sources Sci. Technol. **22**, 015002 (2013).
32) NIST Atomic Spectra Database, https://www.nist.gov/pml/atomic-spectra-database
33) A. Bondi, J. Phys. Chem. **68**, 441 (1964).
34) M. Mantina, A. C. Chamberlin, R. Valero, C. J. Cramer, and D. G. Truhlar, J. Phys. Chem. **113**, 5806 (2009).
35) M. W. Kiehlbauch and D. B. Graves, J. Appl. Phys. **91**, 3539 (2002).
36) A. V. Phelps, J. Phys. Chem. Ref. Data **20**, 557 (1991).

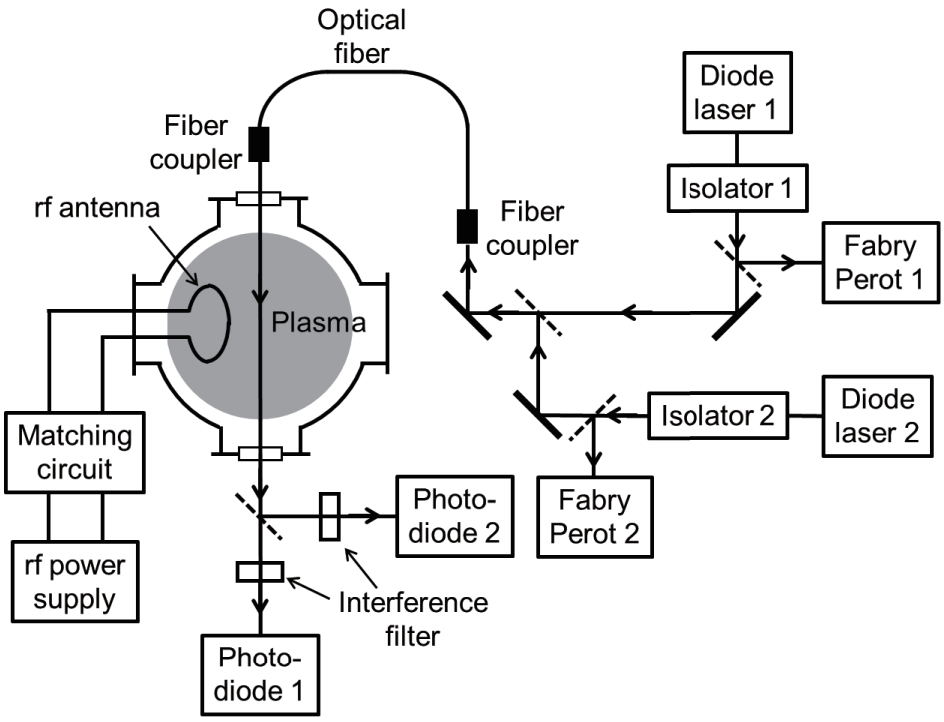


**Fig. 1.** Schematic of experimental setup.

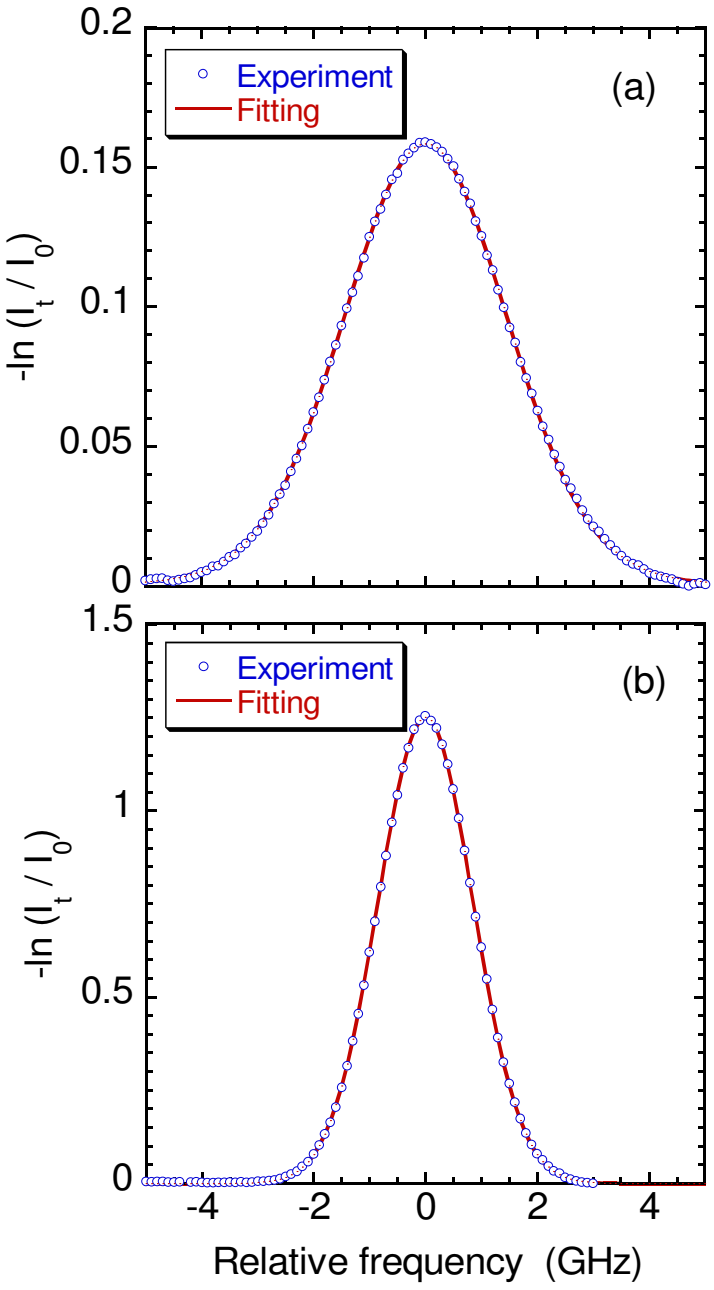


**Fig. 2.** Absorption spectra of (a) ${}^1P_1^o - {}^1D_2$ and (b) ${}^3S_1 - {}^3P_0^o$ transition lines of helium in an inductively coupled plasma with an rf power and a helium pressure of 700 W and 50 mTorr, respectively. The plots show the experimental results, and the solid curves are the fittings using (a) Voigt (b) Gaussian functions, respectively.

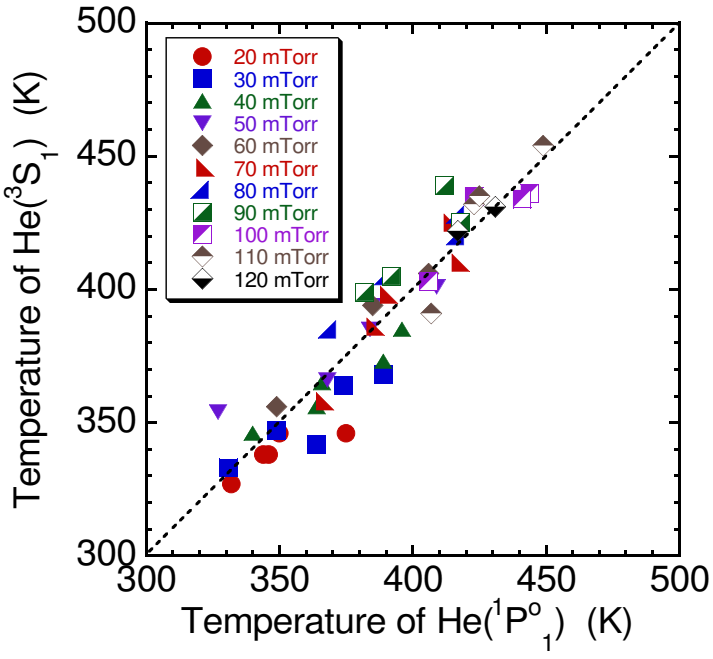


**Fig. 3.** Comparison between the temperatures of He($^1P^o_1$) and He($^3S_1$). The plasmas were produced at rf powers between 300 and 700 W and helium pressures between 20 and 120 mTorr.

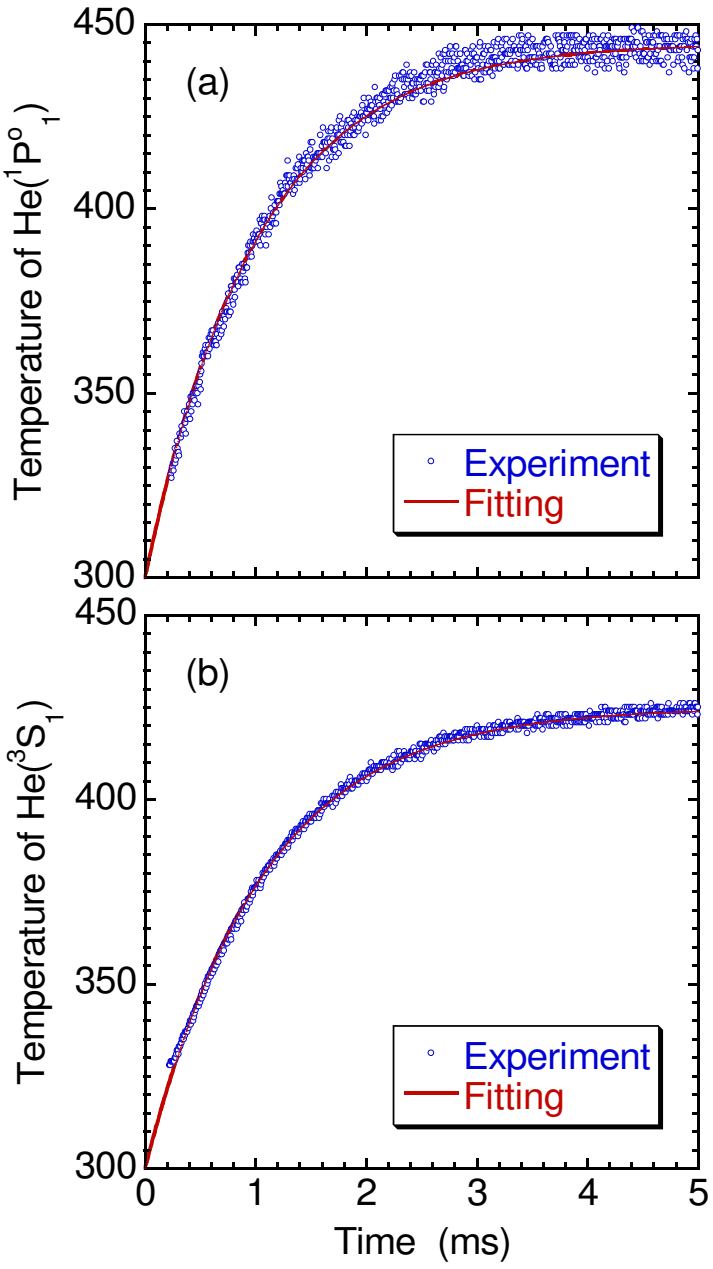


**Fig. 4.** Temporal variations of temperatures of (a) He($^1P^o_1$) and (b) He($^3S_1$) after the initiation of the discharge. The rf power and the helium pressure were 500 W and 80 mTorr, respectively.

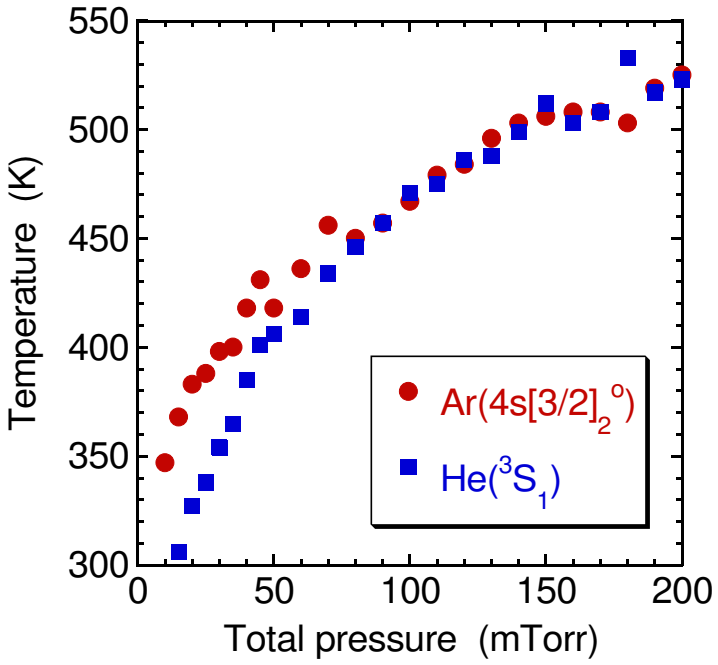


**Fig. 5.** Temperatures of He($^3S_1$) and Ar($4s[3/2]_2^o$) as a function of the total pressure in helium-argon mixture plasmas. The rf power was 500 W and the partial pressure ratio was $P_{\mathrm{He}} : P_{\mathrm{Ar}} = 20 : 1$.

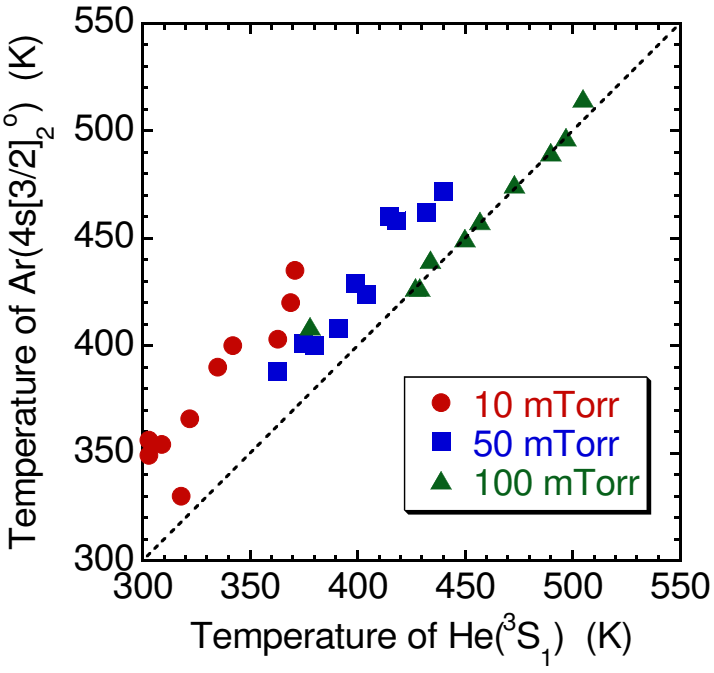


**Fig. 6.** Comparison between the temperatures of He($^3S_1$) and Ar($4s[3/2]_2^o$) at three total pressures of 10, 50, and 100 mTorr. The plasmas were produced at rf powers between 100 and 1000 W.

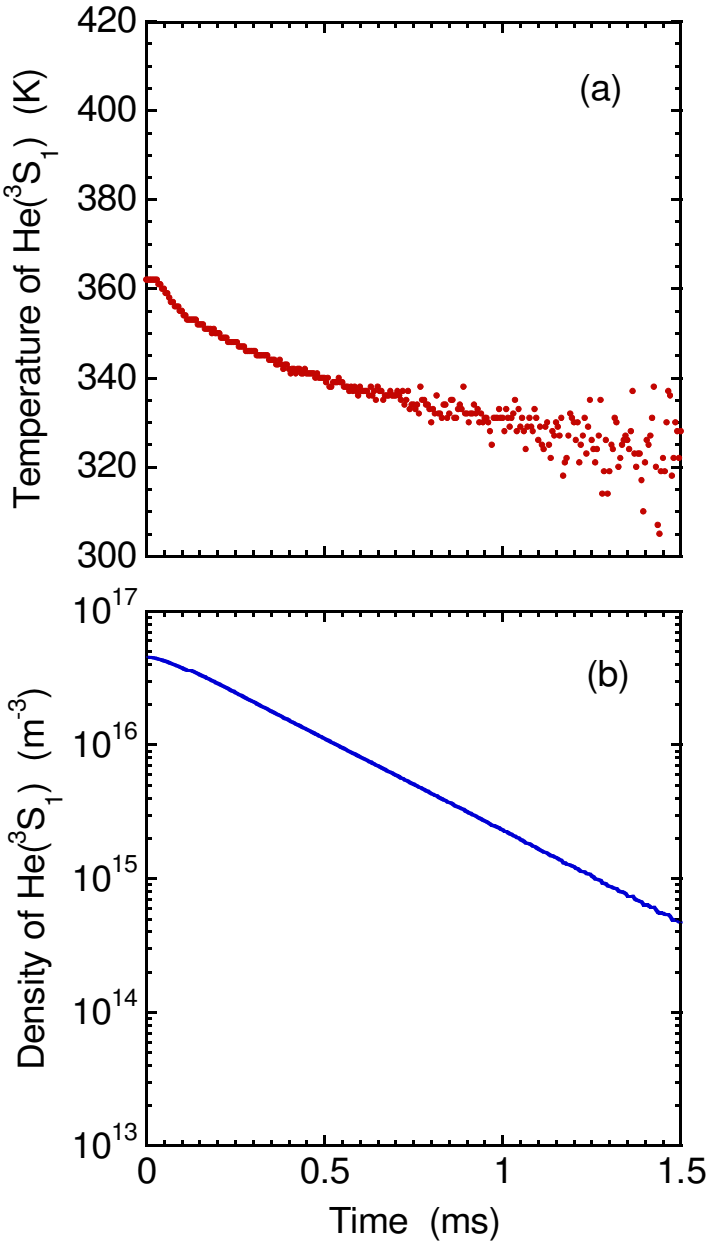


**Fig. 7.** Temporal decreases in (a) temperature and (b) density of He($^3S_1$) in the afterglow of a pulsed helium-argon mixture discharge. The total pressure was 50 mTorr and the rf power in the discharge phase was 200 W.

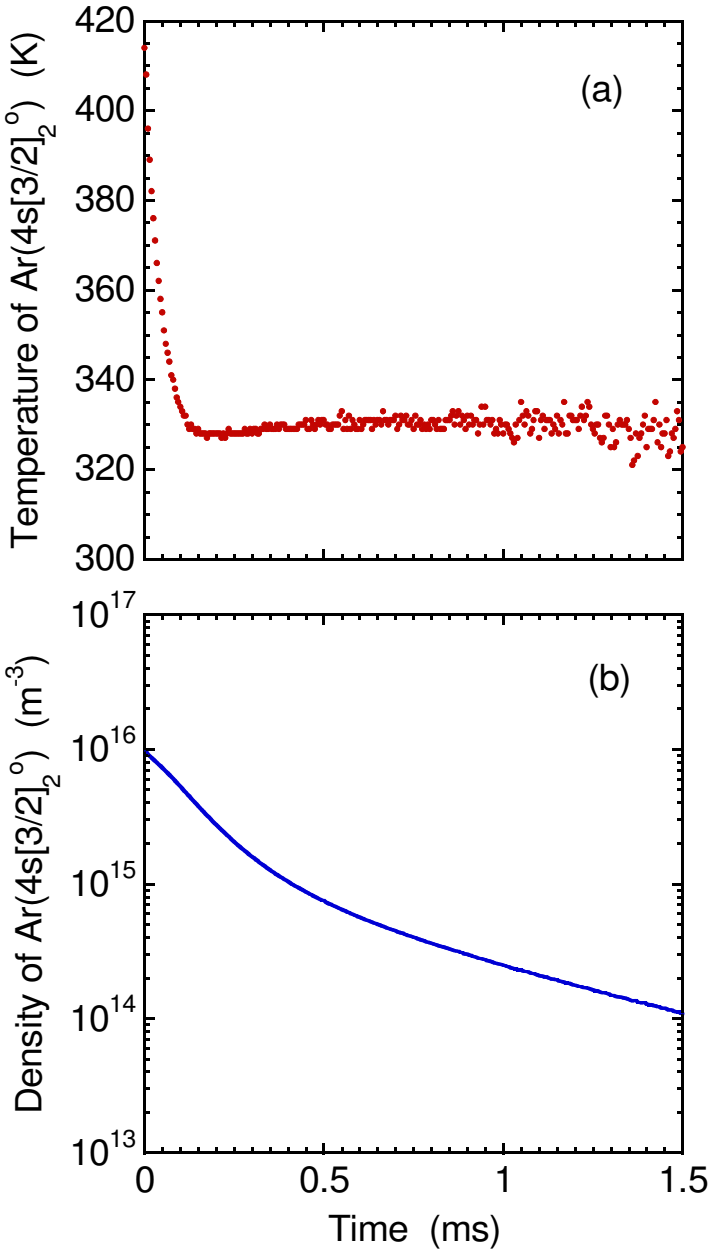


**Fig. 8.** Temporal decreases in (a) temperature and (b) density of Ar($4s[3/2]_2^o$) in the afterglow of a pulsed helium-argon mixture discharge. The discharge conditions were the same as those in Fig. 7.